Vicarious calibration of the Moderate-Resolution Imaging Spectroradiometer Airborne Simulator thermal-infrared channels

Zhengming Wan, Yulin Zhang, Xialin Ma, Michael D. King, Jeffrey S. Myers, and Xiaowen Li

We made an experimental vicarious calibration of the Moderate Resolution Imaging Spectroradiometer (MODIS) Airborne Simulator (MAS) thermal infrared (TIR) channel data acquired in the field campaign near Mono Lake, Calif. on 10 March 1998 to demonstrate the advantage of using high-elevation sites in dry atmospheric conditions for vicarious calibration. With three lake-surface sites and one snow-field site, we estimated the MAS noise-equivalent temperature difference as 0.7–1.0 °C for bands 30–32 in the 3.68–4.13-μm region and 0.1–0.5 °C for bands 42, 45, 46, and 48 in the 8–13.5-μm region. This study shows that the MAS calibration error is within ±0.4 °C in the split-window channels (at 11 and 12 μm) and larger in other TIR channels based on the MAS data over Mono Lake and *in situ* measurement data over the snow-field site. © 1999 Optical Society of America

OCIS codes: 040.3060, 120.0280, 120.0120, 120.5630.

1. Introduction

The Moderate Resolution Imaging Spectroradiometer (MODIS) has been developed as the keystone instrument[1,2] on the Earth Observing System (EOS) Terra (formerly EOS AM-1) platform[3] for global studies of atmosphere, land, and ocean processes.[4–6] To support the validation of MODIS algorithms and data products, the MODIS Airborne Simulator (MAS) has been developed for NASA's high-altitude ER-2 research aircraft as an outgrowth of the development of the Wildfire IR imaging spectrometer that was originally designed for investigations of high-temperature terrestrial targets such as forest fires. Beginning in January 1995, a 50-channel, 16-bit digitizer was used, which greatly enhanced the capability of MAS to simulate MODIS data in a wide range of environmental conditions. The dynamic range of the thermal-infrared (TIR) channels is wide enough to encompass cold cloud targets as well as warm terrestrial surface targets. MAS has a spatial resolution of 50 m (pixel size) at sea level when on the ER-2 research aircraft flying at an altitude of 20 km. Radiometric calibration of the short-wave MAS channels is obtained by observing laboratory standard integrating sphere sources on the ground before and after flight missions, while calibration of the IR channels is performed in flight by viewing two onboard blackbody sources once every scan. King *et al.*[7] described the technical details, calibration method, and performance evaluation of the MAS instrument. The new calibration method takes into account the effect of the measured emissivity of the onboard blackbodies as well as the reflective component of the instrument cavity off the blackbody surfaces. In the preliminary MAS level 1B processing, the calibration of MAS TIR data was based on the effective blackbody emissivity values determined by regression analysis of the laboratory observations of a thermally controlled external source in a stable ambient environment.[8]

The operational calibration of the MAS TIR channels is accomplished through in-flight observations of two onboard blackbody sources and the use of the instrument characteristics (in particular, the blackbody emissivity) determined from preflight calibration activities in the laboratory. Because during flights the MAS performs in a different environment

Z. Wan, Y. Zhang, and X. Ma are with the Institute for Computational Earth System Science, University of California, Santa Barbara, Santa Barbara, California 93106. The e-mail address for Z. Wan is wan@icess.ucsb.edu. M. D. King is with the NASA Goddard Space Flight Center, Greenbelt, Maryland 20771. J. S. Myers is with the NASA Ames Research Center, Moffett Field, California 94035. X. Li is with the Center for Remote Sensing, Boston University, Boston, Massachusetts 02215.

from the laboratory environment and the MAS is a complicated instrument, any unexpected thermal deformation, small changes in its optical alignment, and other factors may affect its calibration performance. Therefore it is necessary to validate the in-flight calibration accuracy and to check the long-term stability of calibration through some calibration means, also known as vicarious calibration.[9] Vicarious calibration is an in-flight or on-orbit technique in which calibrated ground-based or airborne radiometers deployed on or above a spectrally and spatially homogeneous target take simultaneous measurements during periods of aircraft or satellite instrument overpasses.[10] Before an airborne radiometer can be used as a vicarious calibration instrument for other airborne and/or satellite sensors, its calibration accuracy has to be validated and its long-term stability has to be verified. For solar reflective bands, ground-based vicarious calibration activities of Landsat over the area of the White Sands Missile Range[11] and those of the Systeme pour l'Observation de la Terre (SPOT) over the LaCrau test site, France,[12] indicated that the vicarious results should be superior from an absolute calibration point and give calibration information of Landsat and SPOT over periods of months to years.

To validate the calibration accuracy (0.5–1.0%) of the MODIS TIR channels, vicarious calibration requires high accuracy for ground-based measurements of surface-leaving radiance (or surface temperature and emissivity) and for the measurements of atmospheric temperature and water vapor profiles. The reason is that we have to convert the ground-based radiances into the top-of-the atmosphere radiances through radiative-transfer simulations based on measured atmospheric temperature and water vapor profiles to compare them with the measured radiances in the MODIS TIR channels. The overall error associated with uncertainties in ground-based surface parameters and atmospheric profiles, and in the atmospheric radiative-transfer simulation based on measured atmospheric and surface conditions, should be much smaller than 1%. Smith *et al*.[13] showed that the sea surface temperature was measured to an accuracy believed to be better than 0.1 °C with the Atmospheric Emitted Radiance Interferometer (AERI) over the Gulf of Mexico during a five-day oceanographic cruise in January 1995. They showed that for microwindows the narrow windows between absorption lines where the atmospheric effects are small, observed with instruments of high spectral resolution such as the ER-2 High Resolution Interferometer Sounder (HIS), the uncertainty in the calculated top-of-the-atmosphere radiances is weakly dependent on the accuracy of the atmospheric temperature and water vapor profile. However, for other narrow bands of the HIS and for moderate-resolution TIR channels of the MODIS and the MAS this uncertainty may be strongly dependent on the accuracy of the atmospheric temperature and water vapor profile and on the accuracy of the empirical water vapor continuum absorption[14] used in atmospheric radiative-transfer calculations. An effective way to reduce the uncertainty in atmospheric radiative-transfer calculations is to conduct vicarious calibration field campaigns over high-altitude sites in dry atmospheric conditions. This requirement is important for TIR vicarious calibration activities to be a success.

To obtain accurate surface-leaving radiance from ground-based measurements, we need to select suitable test sites and to rigorously calibrate the ground-based instruments before, during, and after field campaigns. Large homogeneous test sites such as silt playas and inland lakes have been chosen because their surface emissivities can be measured or modeled and their *in situ* surface temperatures can be measured more accurately. Because the field-of-view (FOV) of ground-based instruments is much smaller than those of airborne and satellite sensors, the viewing angle and measurements time may not be exactly the same, *in situ* measurements must be made at multiple locations, multiple viewing angles, and multiple times (before and after the overpasses of airborne and/or satellite sensors) to reduce the uncertainties in temporal interpolation, spatial sampling and averaging, and geometric coregistration, to ensure that MODIS/MAS measured radiances can be compared accurately.

Vicarious calibration of MAS TIR channels is also important for the following reasons: (1) It is relatively easier to make *in situ* measurements at the MAS pixel scale than the MODIS pixel (1-km) scale. (2) Once MAS calibration is validated and its long-term stability is established through regular vicarious calibration activities, it can be used to validate the calibration accuracy of MODIS TIR channels. (3) MAS data will be used to validate MODIS land-surface temperature (LST) products in areas with heterogeneous land-cover types in complicated terrains where it is almost impossible to obtain accurate ground-based measurement data at the MODIS pixel scale.

We give in Section 2 a brief description of the TIR instruments used in our vicarious calibration field campaign. We describe the MAS flights and field measurements in the March 1998 field campaign conducted near Mono Lake, Calif. in Section 3 and present the vicarious calibration results in Section 4. Conclusions and the MODIS LST plan for calibration/validation activities are in Section 5.

2. Ground-Based Instruments for Vicarious Calibration

Surface temperature measurements can be made with contact sensors, broadband radiometers, and IR spectrometers. The contact sensors are thermistors with dataloggers for surface temperature measurements of water body and flat land surfaces such as the silt playa 1–2 mm beneath the surface. Temperature is recovered directly from the contact sensors. We use the TIR thermometer manufactured by Heimann as the broadband radiometer. The TIR spectrometer (from MIDAC Corporation) equipped with an InSb/MCT sandwich detector can provide

radiance data at a selectable spectral resolution of 1–32 wave numbers in the spectral range of 3.5–14.5 μm. Normally we select the four-wave-number resolution in our field measurements. At this spectral resolution, the speed of the spectrometer is 8 spectra/s. We made a series of custom improvements to this TIR spectrometer, including installation of a beam expander, a scanning mirror, and three blackbody boxes in the front of the spectrometer. The FOV of this improved TIR spectrometer is approximately 25 cm when it is placed at a platform 3 m above the ground. This TIR spectrometer with the scanning mirror can scan a range of angles to provide temporal and angular spectral surface radiance and atmospheric downwelling irradiance (with a diffuse reflector). The measured downwelling irradiance is used in the atmospheric correction of the ground-based measurement data. These TIR instruments are calibrated with a full aperture blackbody in a range of temperature wide enough to cover the surface temperature conditions in the field. An aluminum-foil cone is placed in front of the blackbody aperture to isolate the blackbody from environmental radiation (also for reducing the stray light effects), and TIR instruments view the blackbody surface through the aluminum-foil cone. We also use a water-bathed cone blackbody to check the accuracies of our TIR instruments (including the full aperture blackbody) routinely. High-precision thermistors (with better than 0.1 °C accuracy) used in the blackbodies provide traceability to the National Institute of Standards and Technology (NIST) standard. The accuracies of thermistors and TIR radiometers are ±0.2 °C. Multiple sets are used to obtain better accuracy. The accuracy of the TIR spectrometer is better than 0.15 °C in the 8–14-μm range. In this spectral range the signal-to-noise ratio of a single spectrum of the TIR spectrometer is larger than 1000. At least 256 sets of spectra are averaged to obtain a high signal-to-noise ratio in the medium wavelength range down to 3.5 μm.

Spectral directional–hemispherical emissivity can be measured with an integrating sphere facility that includes a Fourier-transform IR spectrometer and a 5-in. (12.7-cm) infragold integrating sphere. The spectrometer has sensitivity in both the mid- and the thermal IR, covering all MODIS bands of interest for LST. This instrument is primarily used for emissivity measurements of samples such as snow, ice, water, silt, sand, soil, and vegetation leaves.

3. March 1998 Field Campaign with MODIS Airborne Simulator Flights

We have conducted six field campaigns with MAS flights to validate the MODIS LST algorithms in Railroad Valley, Nev. and in the areas of Mono Lake and Death Valley, Calif. in 1995–1998. Although these field campaigns provided useful data for LST validation purposes (to validate the LST algorithm at 1 °C accuracy), we found that only the data collected in the field campaign conducted near Mono Lake in March 1998 can be used for vicarious calibration of the MAS thermal channels because of the calm clear

Table 1. Central Wavelength (λ_c) and Bandwidth ($\Delta\lambda$) of the MAS Channels as Configured in March 1998 and the Equivalent Channels of the MODIS Onboard the Terra Platform

MAS Channel	λ_c ($\Delta\lambda$) (μm) (nm)	MODIS Channel	λ_c ($\Delta\lambda$) (μm) (nm)	MAS Channel	λ_c ($\Delta\lambda$) (μm) (nm)	MODIS Channel	λ_c ($\Delta\lambda$) (μm) (nm)
1	0.470 (39)	3	0.469 (20)	26	3.116 (155)		
2	0.552 (42)	4	0.555 (20)	27	3.274 (149)		
3	0.654 (52)	1	0.645 (50)	28	3.429 (159)		
4	0.704 (43)	14	0.678 (10)	29	3.589 (154)		
5	0.746 (42)	15	0.748 (10)	30	3.745 (140)	20	3.750 (180)
6	0.828 (44)			31	3.905 (152)	22	3.959 (60)
7	0.870 (42)	2	0.858 (35)	32	4.064 (151)	23	4.059 (60)
8	0.912 (41)	17	0.905 (30)	33	4.222 (157)		
9	0.952 (41)	19	0.940 (50)	34	4.372 (165)	24	4.465 (65)
10	1.620 (52)	6	1.640 (24)	35	4.536 (149)	25	4.515 (67)
11	1.674 (52)			36	4.690 (158)		
12	1.728 (52)			37	4.848 (149)		
13	1.780 (52)			38	4.997 (142)		
14	1.832 (50)			39	5.149 (145)		
15	1.884 (52)			40	5.295 (142)		
16	1.932 (52)			41	5.410 (93)		
17	1.984 (54)			42	8.467 (302)	29	8.550 (300)
18	2.036 (57)			43	9.672 (529)	30	9.730 (300)
19	2.084 (55)			44	10.467 (440)		
20	2.134 (56)	7	2.130 (50)	45	10.975 (490)	31	11.030 (500)
21	2.182 (55)			46	11.969 (420)	32	12.020 (500)
22	2.232 (57)			47	12.860 (410)		
23	2.282 (55)			48	13.274 (460)	33	13.335 (300)
24	2.332 (56)			49	13.813 (560)	35	13.935 (300)
25	2.380 (56)			50	14.266 (430)	36	14.235 (300)

sky and dry atmospheric conditions (details given below).

The MAS in its March 1998 configuration has 50 narrow-band channels shown in Table 1 in the spectral range between 0.47 and 14.5 μm, 10 of the shortwave channels (<2.5 μm) similar to the MODIS reflective channels, and 12 of the emissive channels similar to the MODIS TIR bands at approximately the same wavelength locations including the 7 MODIS TIR bands (bands 20, 22, 23, 29, and 31–33) used in the MODIS LST algorithms.[15,16]

We requested two weeks of MAS flight opportunity for the March 1998 field campaign. The MAS flight lines were selected in the north–south direction, covering Mono Lake, snow in mountains and valleys, and forest areas. Details of the MAS flight lines can be found in flight numbers 98–032 and 98–033 on the web page of the NASA Ames Research Center (http://asapdata.arc.nasa.gov/ames_index.html). Three groups participated in this field campaign, one from the MODIS team, one from the Multiangle Imaging Spectroradiometer (MISR) team, and one group of validation scientists.

On 9 March 1998 the ER-2 Operation Office at NASA Dryden Flight Research Center and the Earth Science Division at NASA Ames conducted a test flight for the MAS instrument after its maintenance service. There was a clear sky on 10 March 1998 with a measured wind speed of less than a half meter per second. The daytime MAS flight passed the Mono Lake area around 11:30 Pacific Standard Time (PST) [19:30 Greenwich Mean Time (GMT)]. Since the sky remained clear until early evening, we decided to conduct the night MAS flight mission on the same day. The night MAS flight passed the same area at around 10 p.m. PST. At that time we observed some light haze moving slowly in the sky, which was more obvious in the far distant mountains. A cloud-mask image of the night MAS data showed cirrus clouds almost throughout the whole area. Two radiosonde balloons were launched, one for the daytime MAS flight, and another for the night MAS flight. The measured atmospheric temperature and water vapor profiles are in Fig. 1. The column water vapor calculated from the profile is 0.32 cm for the daytime flight and 0.38 cm for the nighttime flight. In this study we used only the daytime MAS data to avoid the uncertainty caused by night haze and thin cirrus clouds.

We performed ground measurements at a site in the snow field ~1 km from the crossing of Highways 395 and 120 in the east and 70 m from Highway 120 on the north side. This snow site and other interesting sites are shown in Fig. 2 of the daytime MAS image. We enhanced the MAS band brightness temperature images in bands 30, 42, and 45 with the histogram equalization method and then made a color composite image with bands 45, 42, and 30 as red, green, and blue components (see Fig. 2). The left image (a), composed of 1000 lines with each line containing 716 pixels, covers an area of ~45 km in the north–south direction and 32 km in the east–west
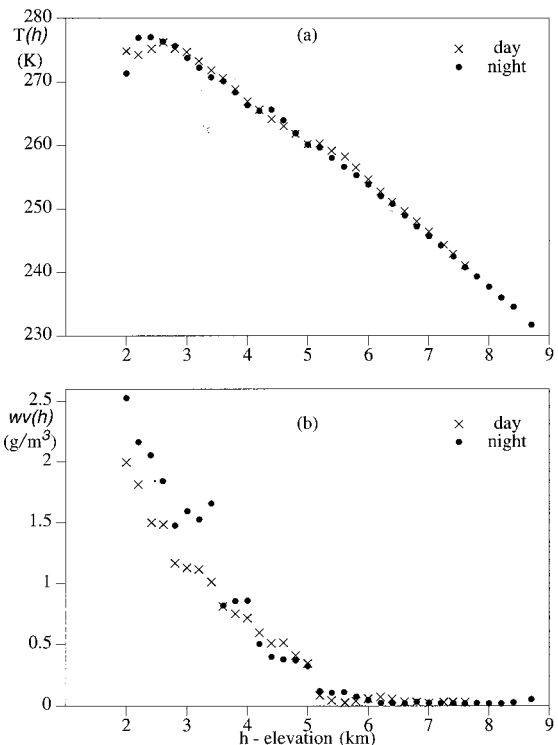

Fig. 1.   (a) Atmospheric temperature and (b) water vapor profiles near Mono Lake, 10 March 1998.

direction. Each pixel represents a spot of approximately 45 m $\times$ 45 m (owing to the surface elevation being approximately 2 km in the region) on the ground. We used one MIDAC Corporation TIR spectrometer to measure temporal TIR radiance from the snow surface. The spectrometer scanned from east to west at viewing angles of 30 to -30 deg in steps of 15 deg. Six broadband radiometers (in a wavelength range of 10–13 μm) were placed 2 m above the surface to measure the snow surface temperature. Six thermistors were placed a few millimeters beneath the snow surface to take the contact measurement of the near-surface snow temperature. The distance between individual radiometers and thermistors was approximately 50 m. We recorded measurement data from these field instruments throughout the day and night on portable computers and dataloggers. The analysis and the comparison of the measurement data from MAS and field instruments can be found in Section 4. Mono Lake, Highways 395 and 120, Mono Craters, and the forest areas are shown clearly in the image. Mono Lake is on the top. Highway 395 is the white line crossing the image from the upper left corner to the lower right corner. The white line crossing Highway 395 in the N–E direction is Highway 120. The white areas with dark points located inside in the middle portion of the image are the Mono Craters. The yellow-gray areas with nonuniform gray levels in the lower right portion are the forest areas. Mono Lake is in light yellow in the color composite image. Figure 2(b), the right image, is the enlarged subarea for four test
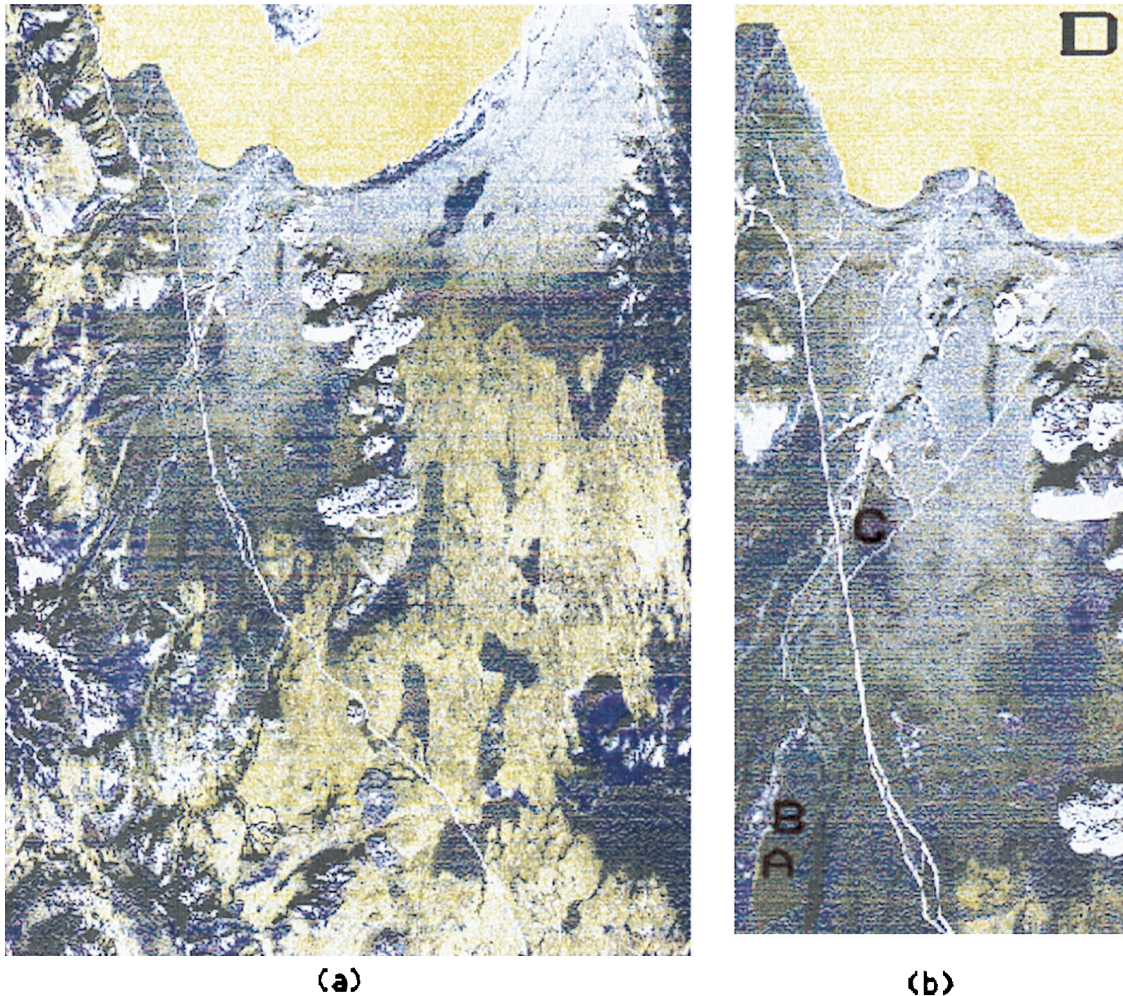
Fig. 2. (a) Color composite with enhanced MAS bands 45, 42, and 30 as red, green, and blue in the Mono Lake area (1000 lines by 716 pixels). (b) Its subareas show four test sites (details in text).

areas used in this study. Grant Lake is in the lower left corner. The lower part in dark gray (labeled A) is the part covered by thin ice, and the upper part in blue (labeled B) is the part covered with snow on 10 March 1998. The near-IR color film taken with a 6-in. RC-10 (CIR) camera on the same ER-2 aircraft carrying the MAS instrument indicates that the thin ice cover on Grant Lake was melting because we can see some strips in the ice area and some small blocks of water surface in black by the edge. The blue area between Highways 395 and 120, in the middle of this image, is the snow-field site (labeled C) where we took field measurements. A portion of Mono Lake (80 × 80 pixels) in the upper right corner (labeled D) is another study area.

4. Results

A. Noise Equivalent Differential Temperature (NEΔT) of MODIS Airborne Simulator Thermal-Infrared Channels

The band brightness temperature is calculated from the pixel radiance value calibrated by the new method,[7] which uses the MAS relative spectral response

functions and corrects the effect of the nonunit blackbody emissivity. The radiance to temperature conversion is given by the adjusted Planck function

$$I_b = B(\lambda_b, \alpha_1 T_b + \alpha_0), \tag{1}$$

where I_b is the band radiance and T_b is the band brightness temperature. The values of the central wavelength λ_b, coefficients α_1 and α_0 for band b, are all given in the MAS level 1B data file.

The focus of this study is on the seven MAS TIR bands (bands 30–32, 42, 45, 46, and 48) that are used in the MODIS LST algorithm. When we investigate other TIR bands, we need measurement data for the atmospheric temperature and water vapor profiles above 9-km elevation above sea level and for other atmospheric parameters including ozone profile, which were not available from this field campaign. To check the radiometric accuracy of the MAS TIR data in these seven bands, we calculated the average band brightness temperatures and standard deviations of the day MAS data over the four flat homogeneous study areas as shown in Table 2. The sizes of

Table 2. Mean and Standard Deviation of Band Brightness Temperature (T_b) and Estimated $NE\Delta T$ in Seven MAS Bands over Four Flat Homogeneous Study Areas in the Mono Lake Field Campaign on 10 March 1998

MAS Band	Band Center (μm)	T_b (δT_b) (°C) Ice-Covered Grant Lake 16 × 16 (A)	T_b (δT_b) (°C) Snow-Covered Grant Lake 16 × 16 (B)	T_b (δT_b) (°C) Snow Site 16 × 16 (C)	T_b (δT_b) (°C) Mono Lake 80 × 80 (D)	Estimated $NE\Delta T_{\min}$	$NE\Delta T_{\max}$ (°C)
30	3.745	−1.49 (1.46)	1.53 (1.29)	2.57 (1.41)	2.78 (1.27)	1.0	
31	3.905	−2.86 (1.14)	−1.40 (1.08)	−0.69 (1.16)	1.79 (0.96)	0.7	
32	4.064	−5.13 (1.39)	−4.28 (1.45)	−4.14 (1.54)	−0.44 (1.27)	1.0	
42	8.467	−3.00 (0.22)	−2.90 (0.22)	−2.87 (0.25)	1.87 (0.34)		0.1
45	10.975	−1.56 (0.25)	−1.42 (0.25)	−1.37 (0.30)	3.97 (0.38)		0.15
46	11.969	−2.81 (0.42)	−2.04 (0.51)	−2.28 (0.53)	3.78 (0.49)		0.3
48	13.274	−10.53 (0.68)	−9.82 (0.63)	−10.05 (0.74)	−6.23 (0.71)		0.5

the study areas are 80 × 80 pixels for the one on Mono Lake and 16 × 16 pixels for the others. The first and second columns of Table 2 contain the band number and band centers λ_b, respectively, while the third through sixth columns are the mean and the standard deviation (in parentheses) of band brightness temperature T_b. The estimated minimum and maximum $NE\Delta T$ values are shown in the last two columns. The possible sources of spatial variations of T_b in each study area include the variations in surface temperature, surface reflectivity, and emissivity and in atmospheric temperature and water vapor profiles. The variations caused by the surface were minimized by the flatness and homogeneity of the selected study areas.

The spectral emissivities of water, snow, and ice are shown in Fig. 3. The water emissivity (solid curve) and ice emissivity (dots) are calculated from the complex index of refraction[17,18] at a MAS viewing angle 1.4° for the Mono Lake study area and 23.2° for ice-covered Grant Lake, respectively. The measured water emissivity (for viewing angle fixed at 10°) is also included to show the quality of our emissivity

Fig. 3. Spectral emissivities of water, snow, and ice in the 3.3–14-μm region.

measurements (maximum error smaller than 0.002 partly due to the small difference between the viewing angles used in calculations and measurements). The measured smooth ice emissivity is not shown in Fig. 3 because of the large effect of changing viewing angle from 10° used in the measurements to 23.2° for the MAS view of ice-covered Grant Lake. The spectral emissivity of snow was obtained by measuring snow samples with our spectrometer-integrating-sphere facility in the cold laboratory at Sierra Nevada Aquatic Research Laboratory (SNARL) on 1 April 1996. According to the daily precipitation data (available from web site http://cdec.water.ca.gov/) collected at the Yosemite headquarters station in the Merced River Basin (~25 miles from Mono Lake), there were snowfalls on 28 and 29 March 1996, and on 5 and 7 March 1998. When we took snow samples by SNARL (20 miles from the snow field near Mono Lake), the snow surface was not touched. A majority of the snow sample was medium-granule snow particles. Although we did not take a snow sample on 10 March 1998 for particle-size and emissivity measurements, it seems reasonable to assume that the snow surface on the snow field near Mono Lake on 10 March 1998 was in a condition similar to the snow sample taken near SNARL for emissivity measurements on 1 April 1996 because both our laboratory measurements of snow emissivity in 1996 and the field measurements of snow surface temperature in 1998 were conducted 3–5 days after snowfalls. Note that the spectral emissivity of snow shown in Fig. 3 is comparable with published data shown in Fig. 4 in Salisbury et al.,[19] and their measurements show that snow emissivity increases owing to the presence of meltwater only at wavelengths near 2.3 and 3.2 μm and in the range from 11 to 13 μm, staying almost the same in the 4–10.5-μm range. Therefore the effect of spatial variations in snow emissivity on the MAS brightness temperature in band 42 over the snow site will be very small. Figure 5 of Ref. 19 shows that the difference between the calculated Fresnel reflectance of ice and the measured directional hemispherical reflectance is very small. We believe that the spatial variation in water emissivity of the Mono Lake surface should be negligible because of the low wind speed. When we
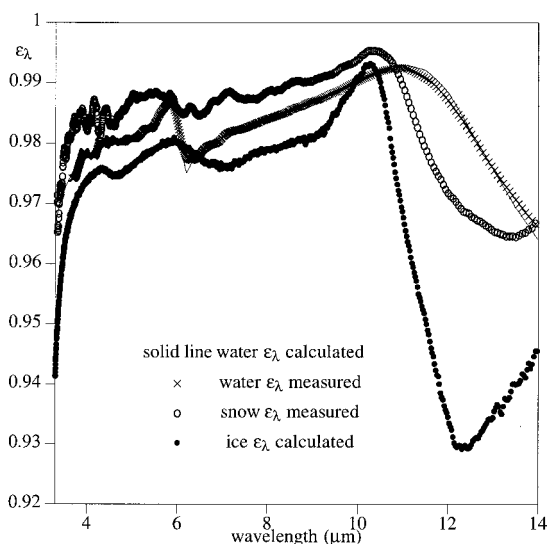
compare the standard deviations of MAS band 42 brightness temperatures (δT_b) over the four study areas shown in Table 2, δT_b over Mono Lake is larger than others. We believe that it is due to the spatial variation in the Mono Lake surface temperature. This also supports the above analysis on the small effect of spatial variations in snow emissivity on the δT_b value in band 42. Because the δT_b values in the row for band 42 ranges from 0.22 to 0.34 °C, we can estimate that half of the smaller value (i.e., 0.1 °C) represents the noise-equivalent differential temperature ($NE\Delta T$) in MAS band 42 with an uncertainty of 0.1 °C. Then we can estimate that the spatial variation in surface temperature is ~0.25 °C for the Mono Lake study area and 0.1–0.15 °C for the ice and snow study areas. Based on these estimated values, we can also obtain the estimated $NE\Delta T$ values for other channels as shown in the last two columns in Table 2. The estimated $NE\Delta T$ values for bands 42, 45, 46, and 48 are comparable with the earlier results based on in-flight measurements over the Gulf of Mexico on 16 January 1995 shown in Table 2 of King et al.,[7] but the $NE\Delta T$ values for bands 30–32 are 2–3 times the earlier results. The reason for the degraded performance of the short-wave IR port (port 3) is under investigation.

Correlation analysis for the study areas also rejected the hypothesis that the major component of the variations in T_b was caused by variations in surface temperature and emissivity. We used the T_b values of each pixel in bands 42 and 30 as independent variables and used the T_b values in other bands as dependent variables. The atmosphere is assumed to be uniform over the study area in this step of the analysis. With T_b of band 42 representing the spatial variation in surface temperature and T_b of band 30 representing the spatial variation in surface reflectivity and emissivity, we expect to find nearly perfect correlation of the dependent variable with the independent variables; i.e., the residual difference between the measured T_b value and the value calculated from the correlation would be small. However, our analysis indicates that it is not true for the T_b data sets of these study areas. By a similar correlation analysis with three independent variables, we can reject the hypothesis that the major component of the variations in T_b was caused by the variation in atmospheric conditions.

B. Effects of Uncertainties in Measured Atmospheric Profiles

We made atmospheric radiative-transfer simulations with version 3.5 of the MODTRAN code[20] for the ice-covered Grant Lake surface (at an elevation of 2 km) based on the atmospheric temperature and water vapor profiles measured during the daytime flight. Above the altitude (8–9 km) at which our radiosonde ceased to provide profile data, we used the standard winter mid-latitude atmospheric profiles in the MODTRAN code. Radiative-transfer simulations showed that the effect of changes in the temperature and water vapor profiles above 9 km is negligible for the

Table 3. Effects of Uncertainties in Atmospheric Profiles on the TOA T_b Values for a Ice-Covered Lake Surface at $T_s = -0.5$ °C According to MODTRAN3.5 Simulations

		Calculated T_b and Sensitivity to $\delta(cwv)$ and δT_a		
MAS Band	Band Center (μm)	Measured Profiles CWV = 0.32 cm	CWV = 0.64 cm No Change in T_a	$T_a + 2$ °C No Change in CWV
30	3.745	−1.30	−1.33 (−0.03)	−1.21 (0.09)
31	3.905	−2.03	−2.03 (0.00)	−1.91 (0.12)
32	4.064	−3.45	−3.45 (0.00)	−3.17 (0.28)
42	8.467	−2.36	−2.49 (−0.13)	−2.16 (0.20)
45	10.975	−1.65	−1.64 (0.01)	−1.60 (0.05)
46	11.969	−3.44	−3.36 (0.08)	−3.38 (0.06)
48	13.274	−12.55	−12.49 (0.06)	−11.98 (0.57)

Note: CWV, column water vapor.

seven MAS TIR bands of interest. We assumed that the thin-ice surface temperature was −0.5 °C and that it reflected solar radiation and downward atmospheric thermal radiative flux as a specular surface. The reflectivity of a smooth ice surface was calculated from the complex index of refraction for ice.[18] The standard rural aerosol profile in the high-visibility condition was used in our simulations. The effect of change in aerosol density in this high-elevation case should be negligible because the atmosphere was so dry and the visibility was extremely high according to our visual observations. The band brightness temperatures (T_b) given by the atmospheric radiative-transfer simulations in the seven MAS TIR bands are in Table 3. The simulated T_b values based on the measured atmospheric profile are given in the third column. The simulated T_b values based on adjusted profiles (one for doubling the water vapor, another for shifting the temperature profile by 2 °C) are given in the next two columns. Because we started the first radiosonde measurement at 10:58 PST and the MAS flight passed the Grant Lake at 11:30 PST, during the 32 min the lower portion of the temperature profile (not just the air surface temperature) may be increased by 2 °C. We can also consider it a possible error in the measured temperature profile. The T_b changes due to adjustments on the column water vapor and temperature profile are shown in parentheses. Owing to the dry atmospheric condition, the effect of doubling the column water vapor on the band radiance at the top of the atmosphere seems to be very small in all seven bands. This effect is evident in the maximum value of −0.13 °C, in band 42, the same level of $NE\Delta T$ in this band. Because of the dry atmosphere and the relatively high surface elevation, the effect of changes in atmospheric temperature profile on T_b appears to be moderate, less than 0.6 °C in band 48 at the worst. If we were to lift the measured atmospheric temperature and water vapor profiles by 2 km so that the surface elevation becomes 4 km above sea level, the effect of changes in atmospheric temperature profile on T_b would be reduced by more than 20% in bands 30–32, 42, and 48. This suggests

that we can make a better vicarious calibration over sites at higher elevations.

Although the ice-covered Grant Lake study area has the minimum values of the standard deviation of MAS T_b in bands 42 and 45–46 as shown in Table 2, we did not use it as a vicarious calibration site because we do not know exactly the surface emissivity of melting ice. But the estimated ice surface emissivity and temperature used in the above atmospheric radiative-transfer simulations are good enough to show the effects of uncertainties in measured atmospheric profiles, especially in dry conditions.

C. Recalibration with Measured Blackbody Emissivity

As described in Eq. (3) in Moeller *et al.*,[8] the equation for nonunit emissivity calibration of MAS thermal IR data in the preliminary MAS 1B processing is

$$R_o = \varepsilon_b \left[(C_o - C_a) \frac{(R_w - R_a)}{(C_w - C_a)} + (R_a - R_r) \right] + R_r, \quad (2)$$

where R_o and C_o refer to observed scene radiance and digital count, R_w and R_a refer to warm and ambient blackbody radiances, C_w and C_a refer to warm and ambient blackbody counts, ε_b represents the effective blackbody emissivity for channel b, and R_r represents the background radiance reflected by the blackbody. The reflected R_r is dominated by radiance from the MAS instrument hardware. In Eq. (2), we omitted the explicit unknown error terms. The value of ε_b (0.98 for short-wave IR channels and 0.94 for long-wave IR channels) was determined by regression analysis of the laboratory observations of a thermally controlled external source in a stable ambient environment.

We measured the spectral emissivity of the Krylon ultraflat black paint that was used to paint the MAS blackbodies and compared it with the spectral emissivity of another Krylon ultraflat black paint sample prepared and measured by the Jet Propulsion Laboratory ASTER (Advanced Spaceborne Thermal Emission Reflectance Radiometer) team (data available as ultra flat black paint 1602.txt from http://speclib.j-pl.nasa.gov/) and the effective emissivities (Table 2 of Moeller *et al.*[8]) in Fig. 4. These two sets of measured spectral emissivity agree well in most of the spectral range from 3 to 13.5 µm. It seems that the differences at 6.5 µm and in the range from 12 to 14 µm are due to the effects of paint thickness and surface smoothness. We found that the differences between the measured emissivity values and the effective blackbody emissivity values in most bands are too large to explain with these effects.

From Eq. (2) the effect of emissivity change on scene radiance is

$$\delta R_o = \frac{\delta \varepsilon_b}{\varepsilon_b} (R_o - R_r). \quad (3)$$

We can calculate R_r from the measured instrument background temperatures (around 17 °C) given in the
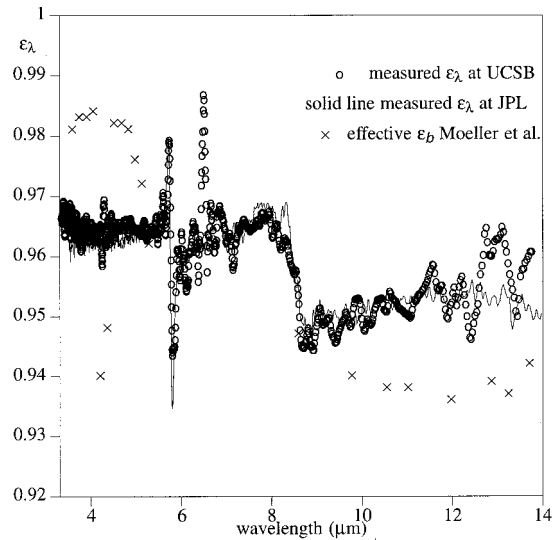

Fig. 4. Spectral emissivities of ultra flat black paint samples measured at University of California, Santa Barbara and JPL and the effective emissivities of the MAS blackbodies.[8]

1B data file. Letting $\delta \varepsilon_b$ be the difference between the measured ε_b and the effective emissivity value, we get the recalibrated scene radiance as

$$R_o' = R_o + \frac{\delta \varepsilon_b}{\varepsilon_b} (R_o - R_r). \quad (4)$$

This permits us to calculate the recalibrated brightness temperature T_b from R_o'. Because the scene brightness temperatures were always lower than the measured MAS instrument background temperature for the four study areas on 10 March 1998, $(R_o - R_r)$ is always a negative number so that the positive or the negative sign of $\delta \varepsilon_b$ will determine whether the scene brightness temperature decreases or increases. As shown in Table 4, this recalibration changed the brightness temperatures in the seven bands by an amount ranging from -0.42 to 0.33 °C over the ice-covered Grant Lake and from -0.31 to 0.20 °C over the Mono Lake study area. Similarly, this recalibration is also made for other study areas. The results are in Table 5. In the case of the Mono Lake study area, the recalibration reduced the maximum and the rms calibration errors in the seven bands by 15% and 11%.

D. Comparison with Ground-Based Measurements over Snow Sites

Six thermistor dataloggers, six TIR thermometers, and one TIR spectrometer were used to measure the snow surface temperature over the snow field between Mono Lake and Grant Lake. With the sunshine causing the snow to melt, the thermistors lost contact with the snow particles. As a result, the thermistors gave the air temperature rather than the snow surface temperature. According to specifications, the Heimann thermometers should work when the ambient temperature is greater than 0 °C and

Table 4. Effect of the Blackbody Emissivity Values on the MAS Calibration in the Ice-Covered Lake and Mono Lake Surface Cases

MAS Band	Band Center (μm)	ε Used in 1B Calibration	1B T_b (°C)	Measured ε of the Black Paint	Recalibrated T_b (°C)	δT_b (°C)
			Ice-Covered Grant Lake Surface			
30	3.745	0.98	−1.49	0.964	−1.25	0.24
31	3.905	0.98	−2.86	0.964	−2.59	0.27
32	4.064	0.98	−5.13	0.964	−4.80	0.33
42	8.467	0.94	−3.00	0.956	−3.24	−0.24
45	10.975	0.94	−1.56	0.951	−1.70	−0.14
46	11.969	0.94	−2.81	0.953	−2.99	−0.18
48	13.274	0.94	−10.53	0.958	−10.95	−0.42
			Mono Lake Surface			
30	3.745	0.98	2.78	0.964	2.91	0.13
31	3.905	0.98	1.79	0.964	1.95	0.16
32	4.064	0.98	−0.44	0.964	−0.24	0.20
42	8.467	0.94	1.87	0.956	1.73	−0.14
45	10.975	0.94	3.97	0.951	3.90	−0.07
46	11.969	0.94	3.78	0.953	3.70	−0.08
48	13.274	0.94	−6.23	0.958	−6.54	−0.31

would not work below 0 °C without heating. Around the MAS overpass time (11:29 am PST), the surface air temperature was around 3 °C. Only three Heimann thermometers worked appropriately, giving the average brightness temperature to be −1.92 °C when the thermometer parameter emissivity was set to 1.0, while the other three gave abnormal data (with sudden excursions). This brightness temperature could be converted into surface radiometric temperature by correcting the effects of surface emissivity and the downward atmospheric radiation. The effect of reflected downward atmospheric radiation is negligible in this case of very dry atmospheric conditions above a surface elevation of 2 km.

The average snow emissivity in the spectral window of Heimann thermometers (10–13 μm) is 0.982, corresponding to a temperature correction of 1.0 °C. After the emissivity correction, Heimann thermometers gave a snow surface temperature at −0.92 °C. The TIR spectrometer gave a snow surface temperature at −0.77 °C at a viewing angle 15° in the spectral

Table 5. Difference between the MAS Brightness Temperature and the TOA Brightness Temperature in Seven MAS TIR Bands (δT_b) over the Three Flat Homogeneous Study Areas[a]

MAS Band	Band Center (μm)	In situ Measurement Derived T_b (°C)	Original T_b (δT_b) (°C)	Recalibrated T_b (δT_b) (°C)
		Snow Field Site at Measured T_s = −0.77 °C (θ_v = 17° and Solar Angle = 42.3°)		
30	3.745	−1.25 to 4.62	2.57	2.71
31	3.905	−1.94 to 1.41	−0.69	−0.47
32	4.064	−3.14 to −1.30	−4.14	−3.83
42	8.467	−2.06	−2.87 (−0.81)	−3.11 (−1.05)
45	10.975	−1.55	−1.37 (0.18)	−1.5 (0.04)
46	11.969	−2.41	−2.28 (0.13)	−2.46 (−0.05)
48	13.274	−10.35	−10.05 (0.30)	−10.45 (−0.10)
		Snow-Covered Grant Lake Surface at T_s = −0.77 °C (θ_v = 23° and solar angle = 42.3°)		
30	3.745	−1.01 to 4.86	1.53	1.69
31	3.905	−1.83 to 1.52	−1.40	−1.16
32	4.064	−3.14 to −1.30	−4.28	−3.97
42	8.467	−2.09	−2.90 (−0.81)	−3.13 (−1.06)
45	10.975	−1.56	−1.42 (0.14)	−1.56 (0.00)
46	11.969	−2.41	−2.02 (0.39)	−2.21 (0.20)
48	13.274	−10.56	−9.82 (0.74)	−10.22 (0.34)
		Mono Lake Surface at T_s = 4.7 °C (θ_v = 1.4° and Solar Angle = 42.3°)		
30	3.745	4.07	2.78 (−1.29)	2.91 (−1.16)
31	3.905	3.20	1.79 (−1.41)	1.95 (−1.35)
32	4.064	1.57	−0.44 (−2.13)	−0.24 (−1.81)
42	8.467	2.64	1.87 (−0.77)	1.73 (−0.91)
45	10.975	3.93	3.97 (0.04)	3.90 (−0.03)
46	11.969	3.70	3.78 (0.08)	3.70 (0.00)
48	13.274	−7.16	−6.23 (0.93)	−6.54 (0.62)

[a]The latter was derived from MODTRAN3.5 simulations based on *in situ* Measurement Data.

range of MAS band 42 (around 8.5 μm) where snow emissivity is around 0.99 and is stable during snow melt so that the effect of the uncertainty in snow emissivity on snow surface temperature is very small. We use the TIR spectrometer measured temperature (-0.77 °C) as snow surface temperature because the TIR spectrometer has better accuracy and the effect of uncertainty in snow emissivity in this narrow spectral range is smaller. The difference between the snow surface temperatures measured by the TIR spectrometer and the Heimann thermometer is 0.15 °C, within the range of uncertainty of Heimann thermometer measurements and the range of the spatial variation of the snow surface temperature measured by MAS. We realize that four measurements are not enough to perform a full analysis of the spatial variation in snow surface temperature at the 1-m scale even though MAS data indicate that surface temperatures over the snow field study area are quite uniform ($\delta T \approx 0.15$ °C) at the 50-m scale. The spatial variation in surface temperatures at a scale of a few meters will be a major concern in future field campaigns.

Atmospheric radiative-transfer simulations were made with the snow temperature measured by the TIR spectrometer and the previously measured emissivity, atmospheric temperature, and water vapor profiles measured by the radiosonde. The MAS viewing angle to the snow field was 17°, and the solar zenith angle was 42.3° at the MAS overpass time. The comparison between the calculated band brightness temperatures (T_b) and the MAS data is shown in the first part of Table 5. For MAS bands 30–32, the calculated T_b values were given in ranges based on the bidirectional reflectance distribution function (BRDF) of the snow in the short-wave range, i.e., how the snow-surface reflects the solar beam. The lower boundary of the T_b range represents the case of a specularly reflecting snow surface so that there is no contribution from the reflected solar beam in the radiance received by the MAS instrument. The upper boundary represents the case in which the snow surface reflects the solar beam, like a Lambertian surface. For the other four MAS bands in Table 5, the effect of the snow's BRDF on the calculated T_b values is negligible in dry atmospheric conditions. Note that the MAS T_b value is the average value of 16×16 pixels, and its precision should be better than 0.1 °C according to the (single-sample) standard deviation values in Table 2. Column 4 in Table 5 contains the T_b value from the original MAS 1B data file. The recalibrated T_b values are given in the last column. The temperature difference (δT_b) between the MAS T_b value and the calculated value is given in parentheses. For MAS channel 45, the δT_b value is smaller than 0.2 °C before recalibration and smaller than 0.05 °C after recalibration. The recalibration has a small effect on bands 45 and 46 because the difference between the measured and the effective emissivities is small in these two bands. This excellent agreement validates the MAS calibration in band 45 within an uncertainty range given by the

error analysis in Subsection 4.F. We adjust surface temperature values for other study areas until δT_b in band 45 is smaller than 0.05 °C (because there is no *in situ* measurement for their surface temperatures).

The comparison over snow-covered Grant Lake is shown in the second part of Table 5. We used the same snow surface temperature measured at the snow field site in atmospheric radiative simulations because the difference in T_b values over these two sites is less than 0.05 °C in bands 42 and 45 as shown in Table 2. The viewing angle was set to 23° corresponding to the MAS look angle.

Note that the δT_b values in bands 46 and 48 changed from the snow-field site near Mono Lake to the snow-covered Grant Lake site. We consider it evidence that snowmelt affects snow emissivity, and there were some differences in snow emissivities over these two snow sites, in the spectral range of 11–13 μm.

E. Results of Vicarious Calibration over the Mono Lake Study Area

The comparison results over the Mono Lake study area are given in the last part of Table 5. As shown in Table 2, the Mono Lake study area has the smallest standard deviation values of band brightness temperature (δT_b) in bands 30–32, whereas δT_b values in bands 42 and 45 are larger than those in other study areas. This indicates that there were some small spatial variations in the lake surface temperature (~ 0.25 °C in the area of 4 km $\times$ 4 km) and that the lake surface would be more like a specularly reflecting surface because of the extreme low wind speed. For a flat water surface, spectral emissivity can be calculated or measured at high accuracies as shown in Fig. 3. In this field campaign we were unable to deploy thermistor dataloggers at desirable locations in Mono Lake owing to the unavailability of boats. We were able to deploy only two thermistors in the lake surface layer near the lake shore. Because there were much larger spatial variations in water surface temperature by the lake shore, we did not select a study site in the area where the thermistors were deployed. After the atmospheric temperature and water vapor profiles were given by *in situ* measurements, the only variable in the inputs to the atmospheric radiative-transfer simulations was the lake surface temperature. With excellent agreement between MAS T_b and the calculated T_b based on measured atmospheric and surface parameters over the snow field study area in band 45, and the maximum $NE\Delta T$ being only 0.15 °C for this band, it is possible to determine the lake surface temperature from MAS observation in band 45 through accurate radiative-transfer simulations. If we set the water surface temperature at 4.7 °C, the calculated T_b values would match well with MAS T_b values within ± 0.05 °C in bands 45 and 46, while the calculated T_b values would be larger than MAS T_b values by 1.2–1.8 °C in bands 30–32. In the atmospheric radiative-transfer simulations, we considered the contribution from the path radiance due to scattering

of the solar radiation and the diffuse solar irradiance reflected by the lake surface, but omitted the contribution from the solar beam reflected by the surface because the lake surface was assumed to be specularly reflecting in low-wind-speed conditions. For information only, the water temperature measured by the two thermistors ~1 cm beneath the surface near the lake shore was 6.6 °C. The 1.9 °C difference represents the spatial variation of the lake surface temperature and the temperature difference for the top 1-cm layer near the lake shore.

It may be argued that the atmospheric temperature and water vapor in the lower boundary layer over Mono Lake could be slightly higher than those measured over the snow-field site, which is ~5 km away from Mono Lake. But these changes cannot improve the overall estimated calibration accuracy because they can make δT_b smaller only in band 48, while δT_b values in bands 30–32 would become even worse.

F. Error Analysis of Ground-Based Thermal-Infrared Measurements

There are two ground-based approaches to obtain the top-of-the atmosphere (TOA) radiance (or band brightness temperature) from *in situ* measurements through atmospheric radiative-transfer simulations. The TOA radiance will be used to compare with MAS or MODIS data for vicarious calibration purposes. The first approach is based on the measured surface emissivity and temperature. The second approach is based on the measured surface-leaving radiance. In the first approach, the uncertainty in measured surface emissivity may be one of the major error sources, depending on the type of land surface. In the second approach, the spectral surface-leaving radiance measured by TIR spectrometers can be directly used as input to the atmospheric radiative-transfer simulations. The most critical part in this approach is that we need the surface-leaving radiance at the MAS or MODIS viewing angle in the whole spectral range of interest at the exact time of the overpass. Currently we take the first approach because we have not found a confident way to separate the measured environmental radiation reflected by the surface into two components, one contributed from the solar and atmospheric radiation, another contributed from the platform that supports the TIR spectrometer. Most recently we made some structural changes in the platform to reduce its platform environmental radiation. If we can separate the second component from the total reflected environmental radiation accurately, we will be able to take the radiance-based approach. Then we will be able to achieve an accuracy of ±0.15 °C, the goal of the MAS vicarious calibration in channels 45 and 46 in ideal surface and atmospheric conditions.

Here we focus on the first approach. If a lake surface is used as a vicarious calibration site, the water surface emissivity can be measured or calculated at an accuracy of better than 0.0025 if the surface is flat in low-wind-speed conditions. Accurate measurements of lake surface temperature and its spatial variations are not easy but are possible with a combination of well-calibrated TIR spectrometers, radiometers, and thermistor buoys. For a snow-field site in our case, the error in snow surface emissivity is the major uncertainty source in step 1 to derive snow surface temperature from TIR radiance and downward atmospheric/environmental irradiance measured by ground-based instruments, and in step 2 to calculate the true land-leaving radiance that is observed by airborne and satellite TIR sensors. If we use the snow-field site as the ultimate vicarious calibration site, we need the snow spectral emissivity at high accuracy in the whole spectral range of interest. This is difficult when the snow surface is in the melting phase as discussed in Subsection 4.A. To avoid the large uncertainty of melting snow emissivity in the 11–13-μm spectral range, we decided to use the Mono Lake study area as our ultimate vicarious calibration site in this experiment and to use the measured snow emissivity and TIR spectrometer measured land-leaving radiance in MAS band 42 to derive the snow surface temperature and then to calculate the TOA radiance at the MAS viewing angle in band 45. By comparing this TOA radiance with MAS band 45 data, we validated that the calibration accuracy of the MAS band 45 is better than 0.10 °C with an uncertainty that will be given in the following analysis.

The calibration accuracy of the TIR spectrometer is better than 0.15 °C. This has been proved by viewing routinely a blackbody at different temperatures. Traceability to the NIST standard is provided by high-precision thermistors that measure the blackbody temperature with an accuracy of better than 0.1 °C. The effect of uncertainties in measured snow surface emissivity in band 42 (less than 0.005) on the surface temperature determination is less than 0.30 °C. Another uncertainty of 0.15 °C is assumed, owing to the residual error after the environmental irradiance reflected by the snow surface is corrected. The rms error of the snow surface temperature is 0.37 °C, which is derived from the radiance measured by the TIR spectrometer and the measured snow surface emissivity. Then we can calculate the TOA radiance based on the measured snow surface emissivity, the derived snow surface temperature, and the measured atmospheric profiles. Note that the effect of the uncertainty in measured snow surface emissivity on the calculated TOA radiance would compensate the effect of the major part of the uncertainty in derived snow surface temperature, which is caused by the uncertainty in the measured snow surface emissivity.

The uncertainty sources in the comparison between the calculated TOA radiance and MAS data in band 45 over the snow field site include the following: (1) The spatial variation in the real snow surface temperature is estimated as 0.15 °C, which is inferred from MAS data over the snow-field study area as shown in Table 2. (2) The effect of the additional uncertainty of snow surface emissivity in band 45 due

Table 6. Comparison of the Calibration Error (δT_b) in the Closely Corresponding TIR Bands of the MAS Configurations in March 1998 and January 1995

MAS Band	Band Center (μm)	δT_b (°C) 10 March 1998 (This Study)	δT_b (°C) 16 January 1995[a]	δT_b (°C) 13 January 1995[b]
30	3.745	-1.2 ± 0.4		
31	3.905	-1.4 ± 0.4	-1.4 (3.90 μm)	
32	4.064	-1.8 ± 0.4		
42	8.467	-0.9 ± 0.4	-0.9 (8.60 μm)	-0.47 (8.59 μm)
45	10.975	0.0 ± 0.4	-0.6 (11.02 μm)	-0.50 (11.01 μm)
46	11.969	0.0 ± 0.4	-0.5 (11.96 μm)	-0.13 (11.97 μm)
48	13.274	0.6 ± 0.4		

[a]Ref. 7.
[b]Ref. 8.

to snow melt (less than 0.005) on the calculated TOA radiance is ~0.30 °C. (3) A residual error of 0.15 °C in the calculated TOA radiance in band 45 after the compensation of the surface emissivity uncertainty and its effect on the derived snow surface temperature. The rms uncertainty in this comparison is 0.37 °C.

Note that in this field campaign we do not have direct *in situ* measurement data for the spatial variation in snow surface temperature at the scale pertaining to the FOV of the spectrometer and for the snow surface emissivity. So there may be an unknown bias in the estimated uncertainty range (± 0.4 °C). We will use an IR camera to measure continuously the spatial distribution of surface temperature in future field campaigns.

G. Cross Comparison of the Calibration of the MODIS Airborne Simulator Thermal Infrared

Table 6 lists the estimated MAS TIR channel calibration errors from this study and two other papers.[7,8] Column 3 is for the MAS configuration in March 1998, and the last two columns are for the MAS configuration in 1995. The values of MAS TIR channel calibration errors in column 3 come from comparison between the recalibrated MAS T_b value and the derived T_b values based on measured atmospheric profiles for the Mono Lake study area, as shown in Table 5, under the assumption that the lake surface temperature can be accurately determined by the MAS channel 45 data. This assumption traces to the vicarious calibration of MAS channel 45 based on *in situ* measurements over the snow-field study area. Therefore an uncertainty of ± 0.4 °C has been added to the estimated calibration errors according to the uncertainty analysis in Subsection 4.F. This uncertainty may be significantly reduced if accurate measurements of lake surface temperatures are available. This study shows that the MAS calibration error for the split-window channels (at 11 and 12 μm) is within ± 0.4 °C while it is larger (from -1.8 to 0.6 °C) in other TIR channels.

In this study we present results from an experimental vicarious calibration of MAS TIR channels for the daytime flight over the Mono Lake study area on 10 March 1998. This vicarious calibration exercise is performed only for a narrow range of scene temperatures (from -1 to 5 °C). However, the significance of this study is shown not only by giving results comparable with those from previous studies based on comparisons with HIS data and giving results for more TIR channels but also by demonstrating the advantages of using high-elevation sites in dry atmospheric conditions as vicarious calibration sites. For such calibration sites, well-calibrated airborne instruments of high spectral resolution are not necessary as long as ground-based instruments can provide accurate spectral surface-leaving radiance or accurate surface temperature and spectral surface emissivity and atmospheric temperature and water vapor profiles at reasonable accuracies. Without requiring a flight of a well-calibrated airborne instrument of high spectral resolution for each ground-based vicarious calibration activity, it will be easy to schedule the calibration field campaigns and to conduct a field campaign at lower cost. Hence it will be possible to conduct more small-scale vicarious calibration field campaigns at different sites.

5. Conclusion

We have presented an economic approach to the vicarious calibration with only ground-based measurements over large flat spectrally and spatially homogeneous sites at high elevations in dry atmospheric conditions. In this study we have shown that the MAS TIR channel calibration may be validated with ground-based measurements at an accuracy of better than 0.5% for channels 45–46 and better than 1% for channels 30–32, 42, and 48 over flat homogeneous test sites in the following conditions: surface elevation above 2 km from sea level, clear skies and low wind speed, column water vapor of less than 0.5 cm, uncertainty in measured atmospheric water vapor profiles of less than 30%, uncertainty in measured atmospheric temperature profiles of less than 2 °C (see Table 3), and surface temperature measured at an accuracy of better than 0.2 °C for test sites in which emissivity is well known from measurements and/or modeling. The vicarious calibration experiment with the MAS data and *in situ*

measurement data collected in the March 1998 Mono Lake field campaign shows that the MAS calibration error for the split-window channels (at 11 and 12 μm) is within ± 0.4 K, whereas it is larger in other TIR channels. We realize that the spatial variation in surface temperatures of test sites is a major uncertainty source in the *in situ* measurements. To reduce the uncertainty in measured surface temperatures we will use an IR camera and more TIR thermometers in future field campaigns. We plan to conduct, in coming years, vicarious calibration activities for MAS and MODIS TIR channels over large flat homogeneous targets at high elevations. Ideal candidate sites of such targets include Namco Lake in Tibet (30.75 °N; 90.5 °E; surface elevation, 4718 m) and Uyuni Salt Flats in Bolivia (20.25 °S; 67.50 °W; surface elevation, 3810 m). We will conduct field campaigns over multiple vicarious calibration sites during the day and at night to validate the calibration accuracy of MODIS TIR channels across a wide range of temperatures. For example, the surface temperature was around -10 °C over the snow-field site near Mono Lake, Calif., at 22:11 PST on 10 March 1998. The daily high and low temperatures over the Uyuni Salt Flats site are around 40 and 15 °C in May.

References

1. V. Salomonson, W. Barnes, P. Maymon, H. Montgomery, and H. Ostrow, "MODIS: advanced facility instrument for studies of the Earth as a system," IEEE Trans. Geosci. Remote Sens. **27,** 145–153 (1989).

2. W. L. Barnes, T. S. Pagano, and V. V. Salomonson, "Prelaunch characteristics of the Moderate Resolution Imaging Spectroradiometer (MODIS) on EOS-AM1," IEEE Trans. Geosci. Remote Sens. **36,** 1088–1100 (1998).

3. M. D. King, D. D. Herring, and D. J. Diner, "The Earth Observing System (EOS): a space-based program for assessing mankind's impact on the global environment," Opt. Photon. News **6,** 34–39 (1995).

4. M. D. King, Y. J. Kaufman, W. P. Menzel, and D. Tanré, "Remote sensing of cloud, aerosol, and water vapor properties from the Moderate Resolution Imaging Spectrometer (MODIS)," IEEE Trans. Geosci. Remote Sens. **30,** 2–27 (1992).

5. C. O. Justice, E. Vermote, J. R. G. Townshend, R. Defries, D. O. Roy, D. K. Hall, V. V. Salomonson, J. L. Privette, G. Riggs, A. Strahler, W. Lucht, R. B. Myneni, K. Knyazikhin, S. W. Running, P. R. Nemani, Z. Wan, A. R. Huete, W. van Leeuwen, R. E. Wolfe, L. Giglio, J.-P. Muller, Y. Knyazikhin, and M. J. Barnsley, "The Moderate Resolution Imaging Spectroradiometer (MODIS): land remote sensing for global change research," IEEE Trans. Geosci. Remote Sens. **36,** 1228–1249 (1998).

6. W. E. Esaias, M. R. Abbott, I. Barton, O. W. Brown, J. W. Campell, K. L. Carder, D. K. Clark, R. L. Evans, F. E. Hoge, H. R. Gordon, W. P. Balch, R. Letelier, and P. J. Minnett, "An overview of MODIS capabilities for ocean science observations," IEEE Trans. Geosci. Remote Sens. **36,** 1250–1265 (1998).

7. M. D. King, W. P. Menzel, P. S. Grant, J. S. Myers, G. T. Arnold, S. E. Platnick, L. E. Gumley, S. C. Tsay, C. C. Moeller, M. Fitzgerald, K. S. Brown, and F. G. Osterwisch, "Airborne scanning spectrometer for remote sensing of cloud, aerosol, water vapor and surface properties," J. Atmos. Ocean. Technol. **13,** 777–794 (1996).

8. C. C. Moeller, P. S. Grant, D. D. Laporte, L. E. Gumley, P. Hajek, W. P. Menzel, J. S. Myers, and S. White, "Blackbody emissivity considerations for radiometric calibration of the MODIS Airborne Simulator (MAS) thermal channels," in *Earth Observing System*, W. L. Barnes, ed., Proc. SPIE **2820,** 44–55 (1996).

9. J. J. Butler and R. A. Barnes, "Calibration strategy for the Earth Observing System (EOS)-AM1 platform," IEEE Trans. Geosci. Remote Sens. **36,** 1056–1061 (1998).

10. P. Slater, S. F. Bigger, K. Thome, D. I. Gellman, and P. R. Spyak, "Vicarious radiometric calibrations of EOS sensors," J. Atmos. Ocean. Technol. **13,** 349–359 (1996).

11. K. Thome, B. Markham, P. Slater, and S. Bigger, "Radiometric calibration of Landsat," Photogram. Eng. Remote Sens. **63,** 853–858 (1997).

12. R. Santer, X. F. Gu, G. Guyot, J. L. Deuze, C. Devaux, E. Vermote, and M. Verbrugghe, "SPOT calibration at the La-Crau test site (France)," Remote Sens. Environ. **41,** 227–237 (1992).

13. W. L. Smith, R. O. Knuteson, H. E. Revercomb, W. Feltz, H. B. Howell, W. P. Menzel, N. R. Nalli, O. Brown, J. Brown, P. Minnett, and W. Mckeown, "Observations of the infrared radiative properties of the ocean—implications for the measurement of sea surface temperature via satellite remote sensing," Bull. Am. Meteorol. Soc. **77,** 41–51 (1996).

14. S. E. Clough, F. X. Kneizys, E. P. Shettle, and G. P. Anderson, "Atmospheric radiance and transmission: FASCOD2," in *Proceedings of the Sixth Conference on Atmospheric Radiation, Williamsburg, Va*. (American Meteorological Society, Boston, 1986), pp. 141–144.

15. Z. Wan and J. Dozier, "A generalized split-window algorithm for retrieving land-surface temperature from space," IEEE Trans. Geosci. Remote Sens. **34,** 892–905 (1996).

16. Z. Wan and Z.-L. Li, "A physics-based algorithm for retrieving land-surface emissivity and temperature from EOS/MODIS data," IEEE Trans. Geosci. Remote Sens. **35,** 980–996 (1997).

17. G. M. Hale and M. R. Querry, "Optical constants of water in the 200-nm to 200-μm wavelength region," Appl. Opt. **12,** 555–641 (1973).

18. S. G. Warren, "Optical constants of ice from the ultraviolet to the microwave," Appl. Opt. **23,** 1206–1225 (1984).

19. J. W. Salisbury, D. M. D'Aria, and A. Wald, "Measurements of thermal infrared spectral reflectance of frost, snow, and ice," J. Geophys. Res. B **99,** 24,235–24,240 (1994).

20. A. Berk, L. S. Bemstein, and D. C. Robertson, "MODTRAN: A moderate resolution model for LOWTRAN," Rep. AFGL-TR-87-0220 (Spectral Sciences, Burlington, Mass., 1987).